# Analysis of non-spherical particle transport in complex internal shear flows

Y. Feng and C. Kleinstreuer

Citation: Physics of Fluids (1994-present) **25**, 091904 (2013); doi: 10.1063/1.4821812
View online: http://dx.doi.org/10.1063/1.4821812
View Table of Contents: http://scitation.aip.org/content/aip/journal/pof2/25/9?ver=pdfcov
Published by the AIP Publishing

PHYSICS OF FLUIDS **25**, 091904 (2013)

# Analysis of non-spherical particle transport in complex internal shear flows

Y. Feng and C. Kleinstreuer[a)]
*Department of Mechanical and Aerospace Engineering, North Carolina State University, Raleigh, North Carolina 27695-7910, USA*

(Received 19 March 2013; accepted 29 August 2013; published online 27 September 2013)

Focusing on ellipsoidal particles of different aspect ratios, the motion characteristics, including critical angle and stable vs. unstable rotational periods, are computationally analyzed in developing and fully developed tubular flows. As an application of particle transport and deposition, the one-way coupled Euler-Lagrange method enhanced by Euler's rotation equations is then employed to simulate laminar-turbulent flow in a subject-specific lung-airway model. First, to gain some basic insight into the dynamics of non-spherical particles, tubular flow is considered where the trajectories of ellipsoidal fibers with randomly initialized incidence angles were released at different inlet-plane positions, computed and visualized. Local and overall particle deposition results are compared between spheres, ellipsoidal fibers, and sphere-equivalent particles for which a revised Stokes diameter was developed. Concerning non-spherical particle transport and deposition in a subject-specific respiratory system, the validated computer simulation model provides realistic and accurate particle-deposition results. Specifically, slender non-spherical particles (i.e., those with higher aspect ratios) are potentially more harmful than thicker ones due to their ability to penetrate into deeper lung regions when somewhat aligned with the major flow field. Furthermore, non-spherical particle deposition is enhanced as the breathing rate increases.
 [http://dx.doi.org/10.1063/1.4821812]

## I. INTRODUCTION

All naturally occurring and most man-made solid particles are non-spherical; for example, air-pollutants, blood cells, drug-aerosols, and industrial particles. Concerning inhaled particles, their size, density, and shape as well as particle interaction phenomena, together with a subject's respiratory tract geometry and breathing pattern greatly determine the fluid-particle dynamics. Although most investigations assumed particles to be perfectly spherical, non-spherical particles, such as fibers, ellipsoids, and disks, exhibit quite different airway trajectories and hence deposition patterns in terms of local wall concentrations and propensity for clearance, or barrier mass transfer into systemic regions. Especially ellipsoids and fibers form a unique class of particles, ranging from toxic fibers found in insulation and packing materials to carbon nanotubes plus multifunctional nanoparticles used as drug-carriers. For example, during inhalation fibers tend to line up with the airflow and hence are more likely to penetrate into the deeper lung regions when compared to spherical particles of the same volume.[1,2] This characteristic indicates that for certain applications an improved drug delivery performance can be achieved using fiber-like carriers.[3,4] It also implies that highly durable, long respirable fibers can be expected to be more toxic than short and less durable respirable fibers, e.g., carbon nanotubes (CNTs)[5–9] which feature high aspect ratios, small diameters, and low solubility. A review of both mathematical models describing fluid-particle dynamics as well as health effects of inhaled toxic particles have been provided by Kleinstreuer and Feng.[10] Simone *et al.*[11] reviewed

[a)]Author to whom correspondence should be addressed. Electronic mail: ck@ncsu.edu

 

toxicity effects of fibers as well as shape engineering for novel drug carriers, while Kleinstreuer *et al.*[12] discussed micrometer- and nano-size drugs for tumor targeting.

The dynamics of ellipsoidal particles is intricate because of the anisotropic shape effect, meaning that the rotational movement must be considered. Ellipsoidal particle transport and deposition in basic shear flows, such as Couette flow and Poiseuille flow, have been investigated experimentally and numerically in order to attain more physical insight of the motion characteristics. For example, Jeffrey[13] studied ellipsoidal particles in linear shear flow and found that the rotation period of the particle is a function of the aspect ratio and flow shear rate. Gallily and Eisner[14] analyzed theoretically and experimentally elongated particles in 2D Poiseuille flow, focusing on the rotation pattern. Chen and Yu[15] proposed a correlation for the fiber sedimentation rate in a horizontal circular tube based on their numerical results. Fan and Ahmadi[16] developed models for ellipsoidal particle transport in channels. In continuation, Shanley and Ahmadi[17] studied ellipsoidal particles in steady flow of a horizontal straight pipe, including motion and sedimentation characteristics, and proposed an empirical correlation for particle deposition. Employing the same numerical model as Fan and Ahmadi,[16] Tian *et al.*[2] claimed that ellipsoidal particles transport motion can be affected by the aspect ratio, flow shear rate, as well as particle density relative to the continuous phase, i.e., air. They also carried out experiments on the deposition efficiency of particles in tubular flow. A similar numerical model was proposed by Yin and Rosendahl[18] but with different expressions for the drag force, the lift force, and the hydraulic torque. They introduced additional assumptions concerning the force expressions when compared to the model built by Ahmadi's research group. Hoeberg *et al.*[19] investigated the Brownian motion effect of submicrometer ellipsoidal particles. Furthermore, Comer and Kleinstreuer[20] investigated the non-sphericity effects of water and n-hexane fuel droplets on the heat transfer mechanisms by numerically calculating the steady laminar axisymmetric thermal flow past solitary oblate spheroids.

Furthermore, a few experimental and numerical methods have been carried out to investigate fiber transport and deposition in human respiratory systems. For example, Myojo[21–23] experimentally studied the deposition of fibers in bronchial airway casts, i.e., single bifurcating tubes based on the 3rd and 4th generation of Weibel's lung model A.[24] Marijnlssen *et al.*[25] measured nylon fiber transport and deposition in lung airways from the trachea to generation 3 and claimed that particle deposition is roughly similar to that of spherical particles, when focusing on the deposition "hot spots" at the carinas. Su and Cheng[26,27] as well as Zhou *et al.*[28] experimentally analyzed the deposition characteristics of different types of fiber material (i.e., CNTs, $TiO_2$, and glass) in two casts of human respiratory systems from mouth to lung airway generation 4. Su and Cheng[26] reported that fibers with lower inertia are more likely to be transported to deeper lung airways, while fibers with higher inertia are more likely to be deposited at the oropharynx wall due to impaction. Also, Su and Cheng[26] stated that the fiber deposition efficiency was generally lower than that of spherical particles. In a follow-up study of their research, Zhou *et al.*[28] also experimentally investigated fiber deposition in tracheobronchial airways with deposition data agreeing well with the results of Sussman *et al.*[29] Su and Cheng[27] proposed several empirical deposition efficiency formulas for fibers depositing in different parts of the human respiratory system from mouth to the first generation. All three papers stated that fiber deposition efficiencies increase with higher Stokes numbers ($St \sim d_{eff}^2$), with $d_{eff}$ being the particle effective diameter. Recently, a novel two-way coupling method has been proposed by Andersson *et al.*[30] for interactions of ellipsoidal particles and turbulent flow. Additional papers on this topic have been reviewed by Kleinstreuer and Feng.[10]

Although a few studies have been carried out for ellipsoidal fibers, their complex movements make it quite difficult to predict patterns of fiber deposition in realistic flow fields. Therefore, it is necessary to gain more physical insight of the dynamics of ellipsoidal fibers. In this study, dilute particle suspensions are assumed, i.e., having volume fractions less than 1%. New physical insight into transport characteristics of ellipsoidal particles in tubular flow is discussed, including a stability analysis on the rotational motion of ellipsoidal particles. The Euler-Lagrange method enhanced by Euler's rotation equations (EL-ER method) was applied for the first time to a realistic human respiratory system (from oral cavity to generation 4) with a new deposition mechanism for ellipsoidal particles. Additionally, a revised Stokes diameter correlation is proposed, based on the numerical simulation results in tubular flow, and validated for inhaled lung-aerosol dynamics simulations.

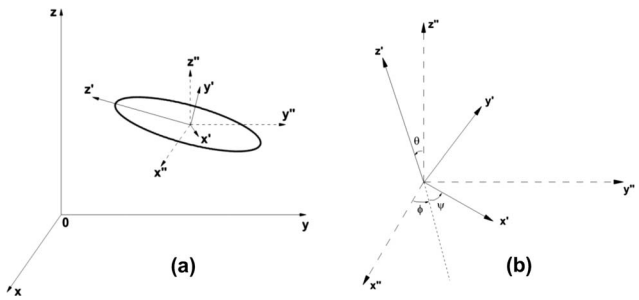


FIG. 1. (a) Coordinate systems for non-spherical particle modeling (b) Euler angles between coordinate x′y′z′ and coordinate x″y″z″.

## II. PROBLEM DESCRIPTION AND NUMERICAL METHOD

The EL-ER method was employed to simulate ellipsoidal fiber transport and deposition in different internal shear flows. In this section, the governing equations of the EL-ER method are discussed in detail. Three different Cartesian coordinates are introduced as well as Euler's quaternions to describe the particle dynamics.

### A. Coordinate transformations and Euler angles

The governing equations of the continuous phase as well as the translation equations for ellipsoidal particles were established in the global coordinate frame, while rotation equations for ellipsoidal particles were given in a body-fixed coordinate frame as follows (see Figures 1(a) and 1(b)):

- *Space-fixed frame xyz:* The inertial coordinate.
- *Body-fixed frame x′y′z′:* The particle coordinate system with its origin being at the particle mass center and its axes being the principal axes (i.e., one major axis and two minor axes of the ellipsoidal fiber).
- *Co-moving frame x″y″z″:* The origin coinciding with that of the body-fixed frame x′y′z′ and its axes being parallel to the corresponding axes of the space-fixed frame xyz.

The transformation from a given Cartesian coordinate system to another can be carried out by means of three successive rotations performed in a specific sequence.[31] For that, the Euler angles ($\varphi$, $\theta$, $\psi$) (see Figure 1(b)), Euler's quaternions ($\varepsilon_1$, $\varepsilon_2$, $\varepsilon_3$, $\eta$), and the transformation matrix A are introduced to facilitate the transformation between different Cartesian coordinate systems. Specifically, the coordinate transformation between axes x′y′z′ and axes xyz can be expressed as

$$\overrightarrow{x'} = A \cdot \vec{x}, \tag{1}$$

in which $\vec{x} = (x, y, z)$, $\overrightarrow{x'} = (x', y', z')$, and $A = [a_{ij}]$ is the transformation matrix.[31] In order to avoid singularity problems, the transformation matrix A has to be rewritten by introducing Euler's quaternions.[31] The Euler quaternions ($\varepsilon_1$, $\varepsilon_2$, $\varepsilon_3$, $\eta$) are defined as

$$\varepsilon_1 = \cos\frac{\phi - \psi}{2}\sin\frac{\theta}{2}, \tag{2a}$$

$$\varepsilon_2 = \sin\frac{\phi - \psi}{2}\sin\frac{\theta}{2}, \tag{2b}$$

$$\varepsilon_3 = \sin\frac{\phi + \psi}{2}\cos\frac{\theta}{2}, \tag{2c}$$

$$\eta = \cos\frac{\phi + \psi}{2}\cos\frac{\theta}{2}. \tag{2d}$$

The Euler quaternions are being used instead of the Euler angles to simulate non-spherical particle kinematics, providing the particle orientation during each time step. Thus, the transformation matrix A[31] can be rewritten as

$$A = \begin{bmatrix} 1-2\left(\varepsilon_2{}^2+\varepsilon_3{}^2\right) & 2\left(\varepsilon_1\varepsilon_2+\varepsilon_3\eta\right) & 2\left(\varepsilon_1\varepsilon_3-\varepsilon_2\eta\right) \\ 2\left(\varepsilon_2\varepsilon_1-\varepsilon_3\eta\right) & 1-2\left(\varepsilon_3{}^2+\varepsilon_1{}^2\right) & 2\left(\varepsilon_2\varepsilon_3+\varepsilon_1\eta\right) \\ 2\left(\varepsilon_3\varepsilon_1+\varepsilon_2\eta\right) & 2\left(\varepsilon_3\varepsilon_2-\varepsilon_1\eta\right) & 1-2\left(\varepsilon_1{}^2+\varepsilon_2{}^2\right) \end{bmatrix}. \tag{3}$$

Detailed discussions of the Euler angles and Euler's quaternions can be found in the dissertation by Feng.[32]

### B. Flow field equations

The governing equations for viscous incompressible, laminar-to-turbulent airflow in a tube, and a subject-specific respiratory tract are given in Zhang and Kleinstreuer.[33] The shear-stress transport (SST) transition model was used, covering an inlet flow rate range of 10 L/min $< Q_{in} <$ 60 L/min, i.e., from sedentary breathing to exercise breathing. While airflow is laminar in the oral region ($Re_{in} <$ 1600), turbulence may occur for $Q_{in} >$ 15 L/min in the larynx, forming a turbulent jet, which typically relaminarizes before the third airway generation is reached.

After solving the Reynolds-averaged Navier-Stokes (RANS) equations, special care has to be applied when recovering the fluid-fluctuation velocities which influence especially nanoparticles in turbulent flow near the wall. Specifically, the fluctuation velocities $v'_{f,i}$ can be expressed as

$$v'_{f,i} = \xi_i \left(\frac{2}{3}k\right)^{\frac{1}{2}}, \tag{4}$$

where k is the turbulence kinetic energy, and the $\xi_i$ values are generated from a Gaussian probability density function of zero mean and unity standard deviation at the start of one eddy-particle interaction. Due to the assumption of turbulence isotropy, the fluctuating velocities normal to the wall calculated with Eq. (4) may be higher than the actual values,[34] leading to over-prediction of particle deposition. To take into account anisotropy and using DNS channel data results, a near-wall ($y^+ < 40$) correction damping function $f_v$ are introduced for the component of fluctuating velocity $v'_{f,n}$ normal to the wall,[34–36] which takes into account the anisotropy effect. It can be expressed as

$$v'_{f,n} = f_v \cdot \xi \cdot \left(\frac{2}{3}k\right)^{\frac{1}{2}}, \tag{5}$$

where

$$f_v = \begin{cases} 1-e^{-0.02y^+} & y^+ < 40 \\ 1 & y^+ \geq 40 \end{cases}. \tag{6}$$

Here, $y^+$ is the dimensionless distance to the wall which is defined as

$$y^+ = \frac{\rho_f \cdot y \cdot u_*}{\mu_f}, \tag{7}$$

where y is the distance to the nearest wall, and $u_*$ is the friction velocity which is defined as

$$u_* = \sqrt{\frac{\tau_w}{\rho_f}} \tag{8}$$

with $\tau_w$ being the local wall shear stress.

### C. Non-spherical particle-trajectory equations

Taking for the present lung-aerosol dynamics case the one-way coupled Euler-Lagrange approach, Newton's second law of translational motion reads in the global xyz-frame[16,37–39]

$$m_p \frac{d\vec{v}_p}{dt} = \vec{F}_D + \vec{F}_L + \vec{F}_{BM} + \vec{F}_g + \vec{F}_{other}. \tag{9}$$

Here, $m_p$ is the mass of the particle, $\vec{F}_D$ is the drag force, $\vec{F}_L$ is the lift force, $\vec{F}_{BM}$ is the Brownian motion induced force, $\vec{F}_g$ is gravity, and $\vec{F}_{other}$ may include interaction forces which have to be considered on a case by case basis. While for spherical particles expressions of acting point-forces are basically established,[40] for non-spherical particles their orientations greatly influence particle trajectories and hence deposition pattern. Thus, Euler's rotation equations combined with the translation equations are necessary for proper particle tracking.[40,41]

#### 1. Drag force

For ellipsoidal particles in Stokes flow, i.e., $\mathrm{Re_p} < 1$, the drag force is

$$\vec{F}_D = \mu_f \pi a_p [K] \cdot \left(\overrightarrow{v_f} - \overrightarrow{v_p}\right). \tag{10}$$

In Eq. (10), $\mathrm{a_p}$ is the semi-minor axis of the ellipsoidal particle, $\overrightarrow{v_f}$ is the fluid velocity vector at the particle centroid, and [K] is the resistance tensor,[42] which in the global xyz-frame can be expressed as

$$[K] = A^{-1} \cdot \left[K'\right] \cdot A. \tag{11}$$

Here [K′] is the resistance tensor in the body-fixed frame x′y′z′. As axes x′, y′, and z′ are the principal axes, [K′] is a diagonal matrix, while the diagonal components can be given by[16]

$$K'_{11} = K'_{22} = \frac{16\left(\beta^2 - 1\right)}{\left[\left(2\beta^2 - 3\right) \cdot \ln\left(\beta + \sqrt{\beta^2 - 1}\right) / \sqrt{\beta^2 - 1}\right] + \beta} \tag{12}$$

and

$$K'_{33} = \frac{8\left(\beta^2 - 1\right)}{\left[\left(2\beta^2 - 1\right) \cdot \ln\left(\beta + \sqrt{\beta^2 - 1}\right) / \sqrt{\beta^2 - 1}\right] - \beta}. \tag{13}$$

Here, $\beta = b_p/a_p$ is the aspect ratio of the ellipsoidal particle and $\kappa_{ii} = \dfrac{K'_{ii}}{6\beta^{1/3}}$ are called "Stokes correction for ellipsoids of aspect ratio $\beta$"[41] or the "dynamic shape factor" which is defined as

$$\kappa_{ii} = \frac{K'_{ii}}{6\beta^{1/3}} = \frac{F_{D,i}}{3\pi d_{eff,v} \cdot \mu_f \left(v_{p,i} - v_{f,i}\right)}. \tag{14}$$

Clearly, $K'_{ii}$ can be replaced using different drag-coefficient correlations.[43,44] It is necessary to emphasize that the drag force for non-spherical particle varies its value according to the change of the particle orientation to the flow. Therefore, the drag force in conjunction with other forces needs to be updated at each time step of the numerical calculation.

#### 2. Lift force

Several expressions for the lift force, $\vec{F}_L$, have been proposed.[38,45–48] Based on the relatively small scale of the ellipsoidal particles when compared to the flow domain ($\dfrac{2b_p}{D_{in}} < 0.02$), a superposition of the lift forces induced by quasi-linear shear flows in different directions was employed.[32] Specifically, the lift force can be considered as a point force and the local flow field around a particle can be considered as the superposition of linear shear flows. As a result, the expression of the lift

force acting on an ellipsoidal particle in a general flow field can be expressed as

$$\vec{F}_L = \sum_{i,j=1}^{3} \vec{F}_L(i,j) \quad (i \neq j), \tag{15}$$

$$\vec{F}_L(i,j) = \frac{\pi^2 \mu_f a_p^2}{\upsilon_f^{1/2}} \cdot \frac{\partial v_{f,i}/\partial x_j}{\left|\partial v_{f,i}/\partial x_j\right|^{1/2}} \cdot \left([K]\cdot[B]_{ij}\cdot[L]\cdot[B]_{ij}^{-1}\cdot[K]\right)\cdot\left(\overrightarrow{v_p} - \overrightarrow{v_f}\right) \quad (i \neq j). \tag{16}$$

Here, i and j denote the three direction of the global coordinates (i, j = 1, 2, 3). $[B]_{ij}$ is the transformation matrix for different velocity gradients. Matrix [L] reads[46]

$$[L] = \begin{bmatrix} 0.0501 & 0.0329 & 0.00 \\ 0.0182 & 0.0173 & 0.00 \\ 0.00 & 0.00 & 0.0373 \end{bmatrix}. \tag{17}$$

### 3. Brownian motion induced force

The Brownian motion induced force will have a significant influence on *nanoparticle* transport. For spherical particles force expressions have been summarized by Longest and Xi.[49] In the present isothermal study (T = 300 K) the Brownian motion induced force for micrometer ellipsoidal particles is employed.[19] As expected, the impact of Brownian motion on the transport and deposition of micrometer-size ellipsoidal particles is negligible.[32]

### 4. Euler's rotation equations

The Euler's rotation equations for ellipsoidal particles in the body-fixed x′y′z′-frame are

$$I_{x'}\frac{d\omega_{x'}}{dt} - \omega_{y'}\omega_{z'}\left(I_{y'} - I_{z'}\right) = T_{x'}, \tag{18a}$$

$$I_{y'}\frac{d\omega_{y'}}{dt} - \omega_{z'}\omega_{x'}\left(I_{z'} - I_{x'}\right) = T_{y'}, \tag{18b}$$

$$I_{z'}\frac{d\omega_{z'}}{dt} - \omega_{x'}\omega_{y'}\left(I_{x'} - I_{y'}\right) = T_{z'}. \tag{18c}$$

Here, $(I_{x'}, I_{y'}, I_{z'})$ are the particle moments of inertia about the principal axes x′, y′, and z′; $(\omega_{x'}, \omega_{y'}, \omega_{z'})$ are the particle angular velocities with respect to the principal axes x′, y′, and z′; and $(T_{x'}, T_{y'}, T_{z'})$ are the torques acting on the particle with respect to the principal axes x′, y′, and z′.

### 5. Hydrodynamics torque

Assuming linear shear flow in the direct vicinity of the micrometer or nano-particle, the torques can be expressed as[32]

$$T_{x'} = \frac{16\pi\mu_f a_p^3 \beta}{3\left(\beta_0 + \beta^2\gamma_0\right)}\left[\left(1-\beta^2\right)D_{z'y'} + \left(1+\beta^2\right)\left(W_{z'y'} - \omega_{x'}\right)\right], \tag{19a}$$

$$T_{y'} = \frac{16\pi\mu_f a_p^3 \beta}{3\left(\alpha_0 + \beta^2\gamma_0\right)}\left[\left(\beta^2-1\right)D_{x'z'} + \left(1+\beta^2\right)\left(W_{x'z'} - \omega_{y'}\right)\right], \tag{19b}$$

$$T_{z'} = \frac{32\pi\mu_f a_p^3 \beta}{3\left(\alpha_0 + \beta_0\right)}\left[W_{y'x'} - \omega_{z'}\right]. \tag{19c}$$

In Eqs. (19a)–(19c), $D_{ij}$ is the deformation rate tensor, and $W_{ij}$ is the spin tensor, given as

$$[D]_{x'y'z'} = \frac{1}{2}\left[\nabla\overrightarrow{v_p} + \left(\nabla\overrightarrow{v_p}\right)^T\right]_{x'y'z'}, \tag{20}$$

$$[W]_{x'y'z'} = \frac{1}{2}\left[\nabla\overrightarrow{v_p} - \left(\nabla\overrightarrow{v_p}\right)^T\right]_{x'y'z'}. \tag{21}$$

Additionally, in Eqs. (19a)–(19c), $\alpha_0$, $\beta_0$, and $\gamma_0$ are

$$\alpha_0 = \beta_0 = \frac{\beta^2}{\beta^2-1} + \frac{\beta}{2\left(\beta^2-1\right)^{3/2}}\ln\left[\frac{\beta-\sqrt{\beta^2-1}}{\beta+\sqrt{\beta^2-1}}\right], \tag{22a}$$

$$\gamma_0 = -\frac{2}{\beta^2-1} - \frac{\beta}{\left(\beta^2-1\right)^{3/2}}\ln\left[\frac{\beta-\sqrt{\beta^2-1}}{\beta+\sqrt{\beta^2-1}}\right]. \tag{22b}$$

In Eqs. (20) and (21), flow velocity gradients in the body-fixed frame can be obtained by transforming the velocity gradients from the global frame. The velocity gradient transformation [G] from the global frame xyz to the body-fixed frame x′y′z′ reads

$$[G]_{x'y'z'} = A \cdot [G]_{xyz} \cdot A^{-1}. \tag{23}$$

The angular velocity components are defined in the body-fixed x′y′z′-frame as

$$\omega_{x'} = \frac{d\psi}{dt} + \frac{d\phi}{dt}\cos\theta, \tag{24a}$$

$$\omega_{y'} = \frac{d\theta}{dt}\cos\psi + \frac{d\phi}{dt}\sin\theta\sin\psi, \tag{24b}$$

$$\omega_{z'} = \frac{d\phi}{dt}\sin\theta\cos\psi - \frac{d\theta}{dt}\sin\psi. \tag{24c}$$

Using Euler's quaternions, Eqs. (24a)–(24c) can be written as

$$\begin{bmatrix} \frac{d\varepsilon_1}{dt} \\ \frac{d\varepsilon_2}{dt} \\ \frac{d\varepsilon_3}{dt} \\ \frac{d\eta}{dt} \end{bmatrix} = \frac{1}{2}\begin{bmatrix} \eta\omega_{x'} - \varepsilon_3\omega_{y'} + \varepsilon_2\omega_{z'} \\ \varepsilon_3\omega_{x'} + \eta\omega_{y'} - \varepsilon_1\omega_{z'} \\ -\varepsilon_2\omega_{x'} + \varepsilon_1\omega_{y'} + \eta\omega_{z'} \\ -\varepsilon_1\omega_{x'} - \varepsilon_2\omega_{y'} - \varepsilon_3\omega_{z'} \end{bmatrix}. \tag{25}$$

### D. Particle deposition mechanisms, numerical solution method, and computer model validations

#### 1. Deposition mechanisms

Because of the anisotropic characteristics of ellipsoidal fibers, non-spherical particle deposition is more complicated than for spheres. For spherical particles, if the distance between the mass center of the particle and the wall is less than the particle radius, deposition will occur, especially for mucus-coated lung airways. However, for ellipsoidal particles the deposition event is more complicated (see Figure 2):

a. If the distance (i.e., $h_p$) between the mass center of the ellipsoidal particle and the inner surface of the wall boundary is less than the semi-minor axis length $a_p$ ($h_p < a_p$), the particle will deposit.
b. If the distance between the mass center of the ellipsoidal particle and the inner surface of the wall boundary is larger than the semi-major axis length $b_p$ ($h_p > b_p$), the particle will not deposit.
c. If the distance between the mass center of the ellipsoidal particle and the inner surface of the wall boundary satisfies the condition $b_p > h_p > a_p$, whether the particle will deposit or not depends on the orientation of its major axis.[32]

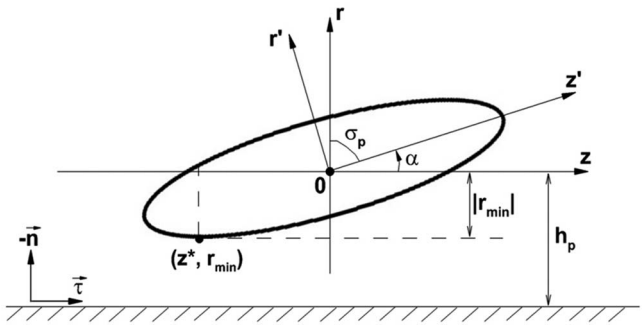


FIG. 2. Ellipsoidal particle deposition sketch.

### 2. Numerical solution

The computational results of the governing equations with appropriate boundary conditions were achieved by using a user-enhanced, commercial finite-volume based program, i.e., ANSYS CFX 13.0 and 14.0 and Fluent 13.0 and 14.0 (Ansys Inc., Canonsburg, PA). The SST transition model in ANSYS CFX 13.0 was employed to solve the laminar-to-turbulence airflow fields. Meanwhile, the translational and rotational motions of the ellipsoidal fibers were solved using in-house user-defined functions (UDFs), which were coupled to ANSYS Fluent Discrete Phase Model (DPM) solver, in order to accurately predict the trajectories of ellipsoidal fibers.

Hexahedral meshes were selected and generated with ANSYS ICEM-CFD. A final mesh of 2,745,600 nodes and 2,698,875 elements was generated and adopted for the present fiber transport and deposition in the Poiseuille flow study. Mesh independence and sensitivity tests were carried out.[32]

### 3. Model validations

To validate the EL-ER method as well as the in-house UDF codes, comparisons with the results by Tian *et al.*[2] for the trajectories of non-spherical particles are presented. A circular duct with L = 700 mm in length and $D_{in} = 4.2$ mm in diameter and an ellipsoidal particle of semi-minor axis $a_p = 0.5$ $\mu$m and an aspect ratio $\beta = 14$ were considered (see Figure 3). A good agreement in magnitude and rotation patterns (i.e., the magnitude of y-direction velocity) between the present numerical calculations and the results of Tian *et al.*[2] are shown in Figures 4(a)–4(d). The reason for the noticeable phase differences between the two results may because of the different densities and viscosities leading to different Stokes numbers used in the two simulations. It should be noted that physical properties of the air were not mentioned by Tian *et al.*[2] Additional reasons for the phase differences include discrepancies in lift force formulations, equation discretization schemes, and solvers used in the two simulations. In any case, it should be noted that the comparisons between our numerical prediction and experimental deposition data (see Figure 5) validated our numerical model well.

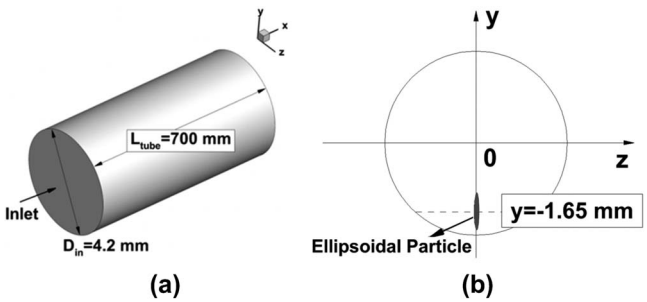


FIG. 3. (a) Sketch of the circular tube (b) initial position of the ellipsoidal particle in the cross-section of the circular tube flow.

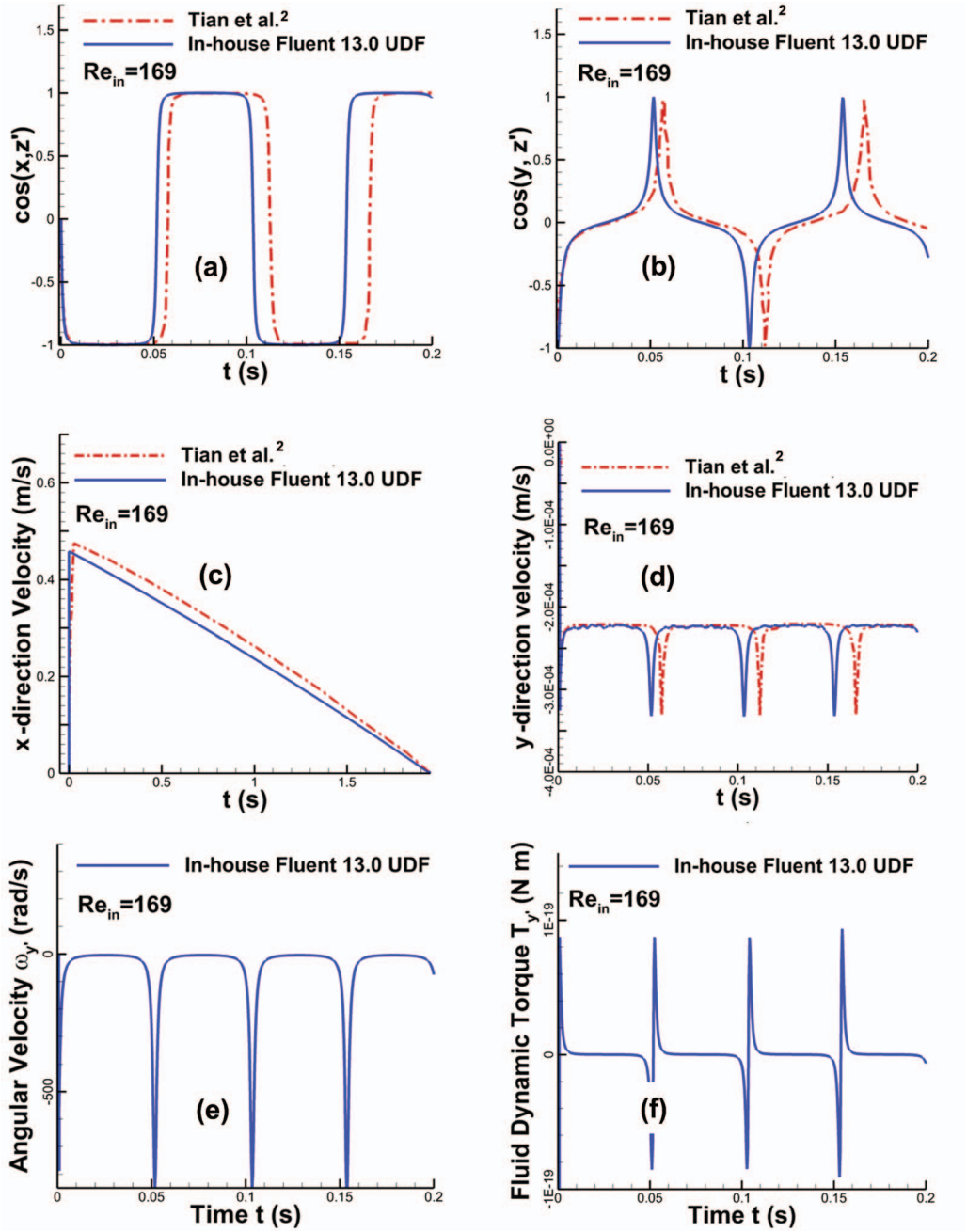


FIG. 4. Comparisons of the ellipsoidal particle transport characteristics with initial injection position (0.3, −0.00165, 0) m between this study and Tian *et al.*[2]; (a) direction cosine between z′- and x-axes; (b) direction cosine between z′- and y-axes; (c) particle axial velocity (x-direction); (d) particle sedimentation velocity (y-direction). (e) particle angular velocity $\omega_{y'}$ vs. time t in Poiseuille flow (f) fluid dynamic torque $T_{y'}$ vs. time t in Poiseuille flow.

In order to validate the model's ability to predict terminal locations of fibers, deposition efficiencies for a single bifurcation have been performed.[32] Assuming a uniform inlet velocity and 100 000 randomly distributed fibers, Figure 5 illustrates comparisons between numerical computations with inlet Reynolds number $Re_{in} = 500$ and existing numerical and experimental data sets in the Stokes number range of $0.005 \leq St \leq 0.5$. The comparisons indicate that our numerical results agree well with the numerical results of Zhang *et al.*[50] for the entire Stokes number range. A broad experimental

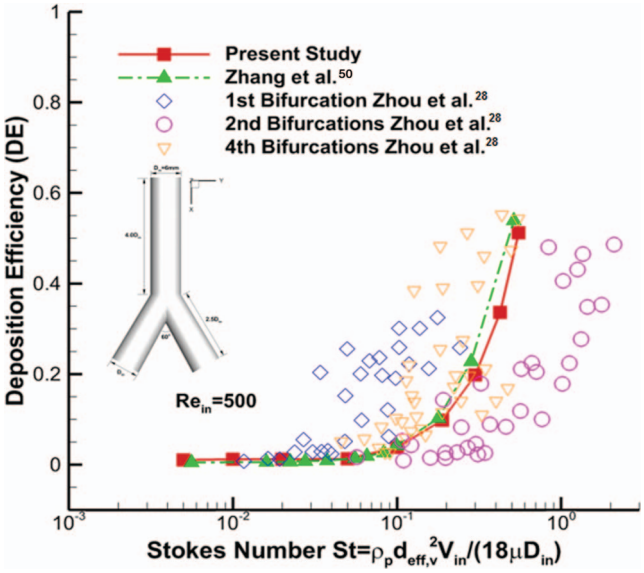


FIG. 5. Comparisons between the fiber deposition efficiencies in the single bifurcation of present study and existing numerical results and experimental data.

data spread[28] can be expected because of different airway geometries and operational conditions employed as well as a relatively high degree of experimental uncertainties.

## III. RESULTS AND DISCUSSION

Considering transport phenomena in tubular and subject-specific airway geometries, new physical insight into the fluid-particle dynamics of ellipsoidal fibers in internal shear flows is provided. Specifically, for tubular flow the concept of "critical angle" in ellipsoidal particle transport is introduced in conjunction with parametric analyses for the transport and deposition of ellipsoidal particles. In order to significantly reduce excessive computer resources when simulating the inhaled aerosol-dynamics in subject-specific lung airways, an improved sphere-equivalent expression (i.e., the revised Stokes diameter) for non-spherical particle deposition is proposed.

### A. Particle motion in Poiseuille flow

For a particle with $a_p = 0.5\ \mu$m and $\beta = 14$ whose initial injection position is x = 0.3 m, y = −0.00165 m, and z = 0 (Figure 3(b)), the translational and rotational motions can be described, using cos(x, z′) and cos(y,z′) x-direction and y-direction velocities, respectively (Figures 4(a)–4(d)). According to Figures 6(a) and 6(b), the particle will be aligned with the flow direction during most of the transport time; however, it will periodically make a sudden 180° rotation as shown. Due to a decrease in vertical drag during the particle-orientation parallel to gravity, the y-direction sedimentation velocity is higher when the particle is parallel to the gravitational direction. Although it seems that the major z′-axis of the particle is parallel to the x-axis most of the time during transport, it is observed that the particle never stops rotating around the y′-axis. It rotates very slowly when the angle between the z′- and x-axes is very small (i.e., around the parallel position), while it rotates very fast when the angle between z′- and x-axes is larger than a *critical value* (Figures 4(a) and 4(b)). As shown in Figure 4(e), the magnitude of the angular velocity is highest when the particle is aligned perpendicular to the flow direction, and decreases as the particle becomes parallel with the flow direction.

The gained physical insight of these special rotational patterns of an ellipsoidal particle is as follows:

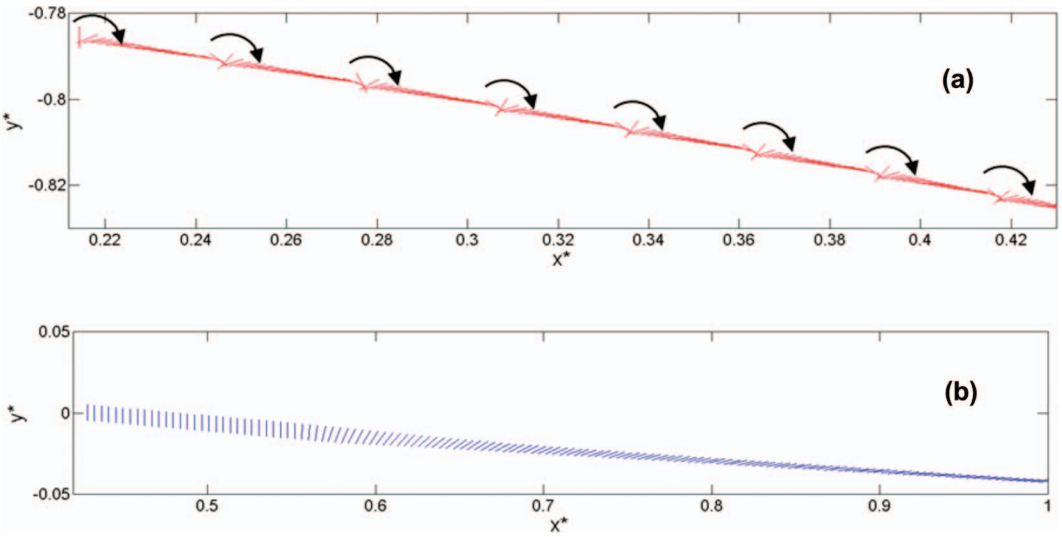


FIG. 6. (a) Ellipsoidal particle z′-axis directions during the transport in the circular tube ($a_p = 0.5\ \mu$m, $\beta = 14$, $Re_{in} = 173$, Injection position x = 0.15 m, y = −0.00165 m, z = 0.0 m) (b) ellipsoidal particle z′-axis directions during the transport in the circular tube ($a_p = 0.5\ \mu$m, $\beta = 14$, $Re_{in} = 173$, Injection position x = 0.3 m, y = 0.0 m, z = 0.0 m). For better visibility, the fiber length was exaggerated in both graphs.

- During the transport, the fluid hydrodynamic torque (see Eqs. (19a)–(19c)) is exerted on the particle and causes the particle to rotate. When the particle rotates at a position which is very close to the position that is parallel to the x-axis, the torque is very small (see Figure 4(f)). Therefore, both angular velocity and angular acceleration are very small which are the reasons why the particle can stay along a quasi-parallel direction (i.e., cos(x, z′) is nearly ±1 and cos (y, z′) is nearly zero) for an extended interval.
- When the particle slowly rotates and exceeds a critical angle $\alpha_{cr} \in [0, 90^\circ]$ between the z′- and x-axes, the torque will drastically increase in magnitude (see Figure 4(f)), leading to a sudden increment of the angular velocity and a sudden 180° rotation of the particle; hence, a new quasi-parallel direction is reached. The sudden torque increase is due to the increase in flow velocity gradients, which leads to an increase in the y′-directional torque acting on the particle. Similar ellipsoidal particle motions were also observed by Tian *et al.*,[2] Shanley and Ahmadi,[17] Hoegberg *et al.*,[19] and Gallily and Eisner,[14] without detailed discussions of the critical angle $\alpha_{cr} \in [0, 90^\circ]$. For a somewhat continuous visualization purpose, Figure 6(a) shows the rotational/translational motions of the ellipsoidal particle released at position x = 0.15 m, y = −0.00165 m, z = 0.0 m in the circular tube during the first 0.25 s.

The coupling of rotation and translation of the ellipsoidal particle can be clearly observed with the periodically sudden "clockwise" 180° turns. The coordinates in Figure 6, i.e., x* and y*, are non-dimensionalized as

$$x^* = \frac{x}{L}, \tag{26}$$

$$y^* = \frac{2 \cdot y}{D_{in}}, \tag{27}$$

$$z^* = \frac{2 \cdot z}{D_{in}}. \tag{28}$$

Figure 6(b) provides another example for the rotational motion of the ellipsoidal particle which was released initially parallel to y-axis at position x = 0.3 m, y = 0.0 m, z = 0.0 m. Due to gravity, the particle was gradually descending. At the initial position, the flow velocity gradients were zero, i.e., no torques were affecting the particle. As a result, the particle kept its initial orientation till it

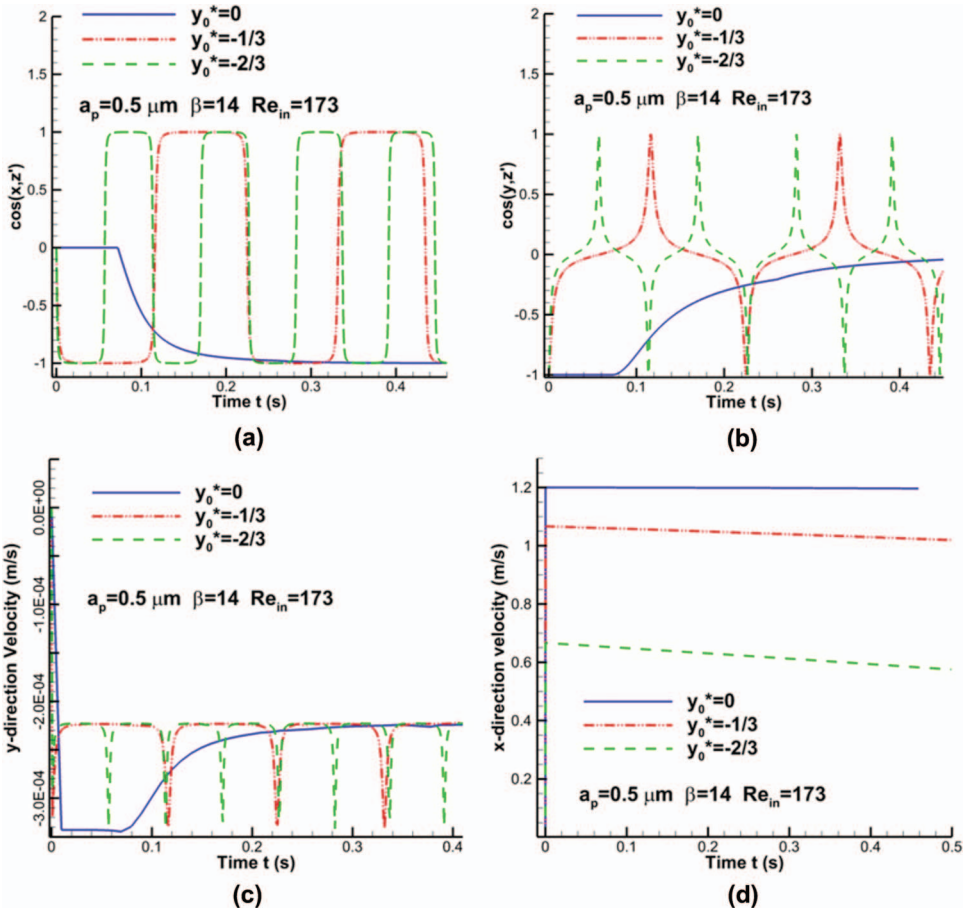


FIG. 7. Motions of particles with different injection positions: (a) direction cosine between z′- and x-axes; (b) direction cosine between z′- and y-axes; (c) particle axial velocity (y-direction); (d) particle sedimentation velocity (x-direction).

reached a location where the velocity gradients and torques were large enough to rotate the particle. The particle started to rotate to the orientation, which was parallel to the x-axis.

Based on the investigations so far, characteristics of an ellipsoidal fiber's transport and deposition in Poiseuille flow can be described mainly in terms of the flow-induced transition, 180° rotation, the rotation period, and the sedimentation velocity. Figures 7–11 depict results of a multi-parameter analysis for the motion of ellipsoidal fiber.

### *1. Initial in-plane release position (z = 0)*

The particle release position (PRP), i.e., where to launch the particle into distinct local shear stress fields, greatly affects the particle motion. Four non-interacting particles were tracked after being released from plane z = 0 and initially parallel with gravity (i.e., the y-axis) with initial non-dimensional y-coordinates $y_0^* = 0$, $-1/3$, $-2/3$, and $+2/3$ (see Eq. (27)). The results during the first 0.45 s are shown in Figures 7(a)–7(d). Additionally, for better visualization of the curves, Figures 8(a)–8(d) show the motion of particles released at $y_0^* = 0$, $+2/3$, and $-2/3$. It can be observed that the rotation frequency of the particles increases as the distance decreases between the particle's released position and the pipe wall. Specifically, due to the higher shear stress near the pipe wall, the magnitude of the hydraulic torque affecting the particle varies faster. As a result, the particle injected near the wall (i.e., $y_0^* = +2/3$, or $-2/3$) is more perturbed and destabilized, leading to a higher sudden rotation frequency. For the particle released at $y_0^* = 0$, a similar pattern of movement was observed when compared to Figure 8. As shown in Figures 7(a) and 7(b), with the particle's

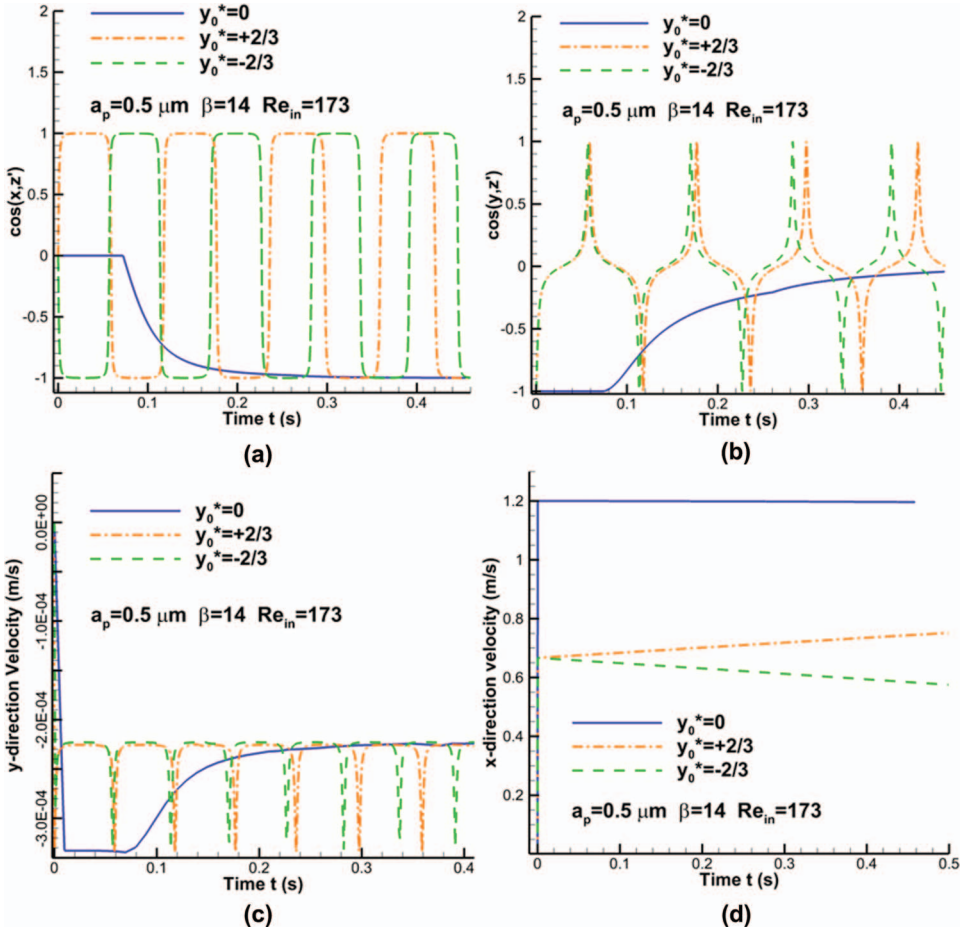


FIG. 8. Motions of particles with different injection positions: (a) direction cosine between z′- and x-axes; (b) direction cosine between z′- and y-axes; (c) particle axial velocity (y-direction); (d) particle sedimentation velocity (x-direction).

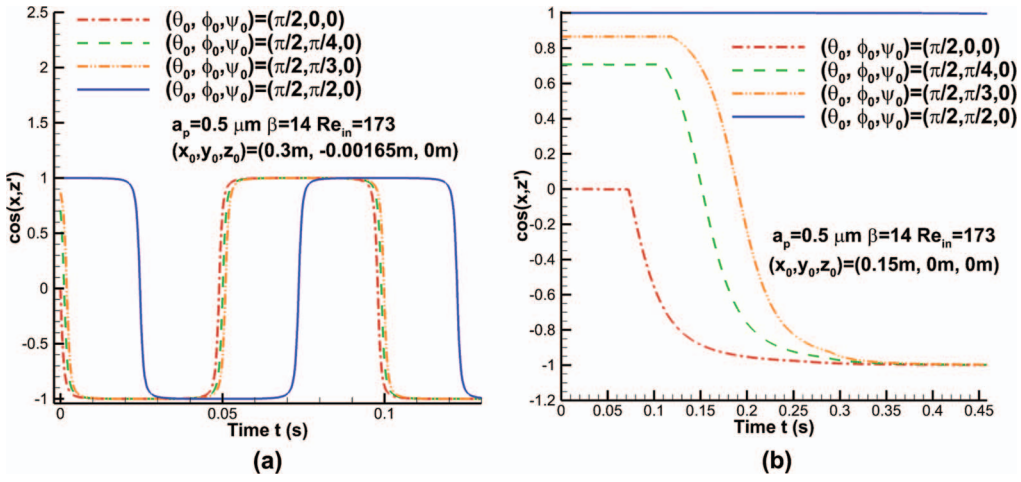


FIG. 9. (a) Direction cosines between z′- and x-axes for particles with different initial Euler angles released at x = 0.15 m, y = −0.00165 m, z = 0.0 m (b) direction cosines between z′- and x-axes for particles with different initial Euler angles released at x = 0.15 m, y = 0.0 m, z = 0.0 m.

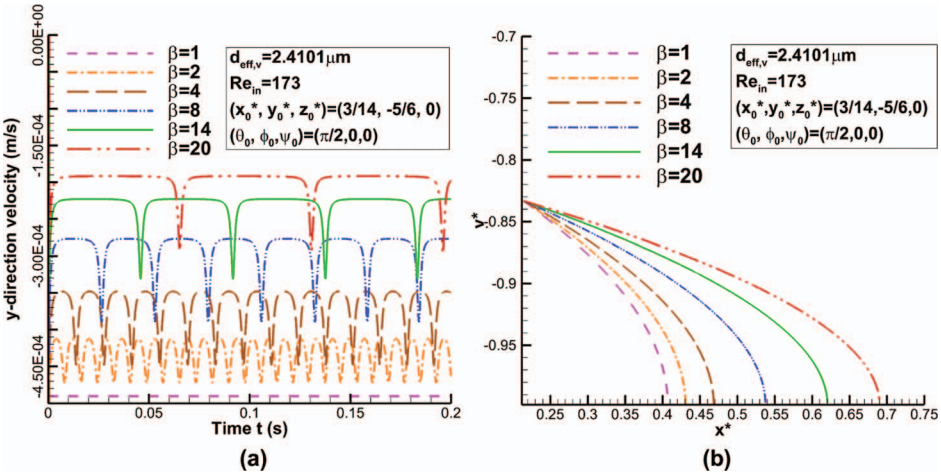


FIG. 10. (a) y-direction velocities of particles with the same volume and different aspect ratios (b) trajectories for ellipsoidal particles with the same volume and different aspect ratios.

sedimentation, the flow velocity gradient at the particle's position will increase which cause the exerted torques to increase. After the torque has reached a critical value, the particle will start to rotate. With the particle orientation gradually changing from parallel to perpendicular, following the gravitational -y direction, the magnitude of the sedimentation velocity (y-component) of the particle decreases (see Figure 7(c)). Such a phenomenon occurs because of the greater drag force in the y-direction when the particle is perpendicular to the gravitational vector rather than parallel to it.

### 2. Initial Euler angles

As expressed in Eqs. (19a)–(19c), components of the hydraulic torque are influenced by the elliptical particle orientation. Therefore, initial Euler angles of the ellipsoidal particle will affect the transport and deposition of the particle. Two groups of particles with different initial Euler angles were investigated and discussed as follows.

Figure 9(a) presents cos(x,z′) values for particles of Group 1 released at x = 0.15 m, y = −0.00165 m, z = 0.0 m with different Euler angles which are specified in the figure legend. For the particle initially parallel to the x-axis, i.e., $(\theta_0, \phi_0, \psi_0) = \left(\frac{\pi}{2}, \frac{\pi}{2}, 0\right)$, the particle is able to move quasi-parallel to the x-axis at the beginning of sedimentation. The periodical sudden 180° turns will occur after the particle is destabilized. For the other three particles, which are not

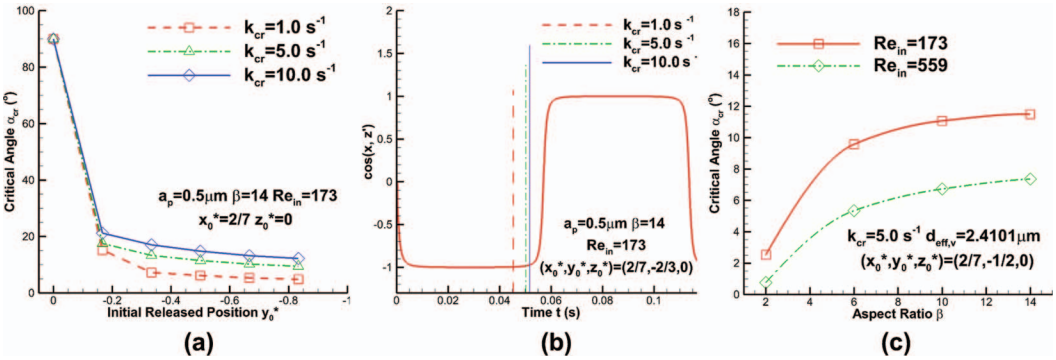


FIG. 11. (a) The relationship between the critical angle defined by different criteria and initial released position (b) comparisons of different threshold of unstable interval $t_{cr}$ using different definition criteria of $k_{cr}$. (c) The relationship between critical angle and inlet Reynolds number as well as particle aspect ratio.

parallel to the x-axis, periodical rotational motion is well observed. The phase differences due to the differences in initial Euler angles ($\phi_0 = 0$, $\phi_0 = \frac{\pi}{4}$, and $\phi_0 = \frac{\pi}{3}$) can be neglected.

Figure 9(b) presents cos(x,z′) values for particles of Group 2, released at x = 0.15 m, y = 0.0 m, z = 0.0 m with different Euler angles which are specified in the legend. For the particle with initial Euler angles $(\theta_0, \phi_0, \psi_0) = \left(\frac{\pi}{2}, \frac{\pi}{2}, 0\right)$, meaning parallel to the x-axis, it rotates at a negligible angular velocity and remains quasi-parallel to the x-axis until escaping from the pipe. For the other three particles shown in Figure 9(b), the angle between x- and z′-axes decreases with an increase in $\phi_0$. These three particles which are not initially parallel to the x-axis will keep their initial direction for some time at the beginning of sedimentation. When the particle descends in the y-direction past a critical point, the particle starts to rotate to the orientation parallel to the x-axis. According to Figure 9(b), the smaller the angle between the x- and z′-axes is, the longer it will be able to maintain its initial orientation during the starting period of sedimentation.

In summary, as shown in Figures 9(a) and 9(b), the ellipsoidal particles which are injected with different initial Euler angles tend to be aligned at orientations which are quasi-parallel to the main axial flow direction, i.e., the x-direction.

#### 3. Aspect ratio $\beta$

Particles with the same equivalent volume diameter and different aspect ratios form significantly different shapes,[32] where $\beta = 1$ represents spherical particles.

Figure 10(a) shows different y-direction velocities of particles with the same volume but different aspect ratios. With the increase of aspect ratio $\beta$, the y-direction sedimentation velocity decreases and the rotation frequency of the particle decreases. Indeed, with different aspect ratios, the Stokes resistance correction factors in the three principal directions of the ellipsoidal particle are all changing, which leads to the variation of the sedimentation velocity in y-direction.

Figure 10(b) provides different trajectories of particles with the same volume and different aspect ratios. Particles with larger $\beta$-values are more able to follow the mainstream and hence travel farther than a particle with a smaller $\beta$. Therefore, it can be conjectured that for the particles with the same volume, fibers are more able to migrate deeper into the lung airways when compared to spherical particles of the same volume. In other words, when quasi-aligned to the flow, a fiber experiences a larger drag force in the gravitational direction (i.e., y-direction), so that particles with larger aspect ratios may not deposit in parallel flow.

### B. Stability analysis of particle rotational motion

#### 1. Critical angle

Based on the rotation patterns, we divided the particle rotational motion into two sessions, i.e., a stable session and an unstable session. In the stable session, a particle rotates at a small angular velocity and with small angular acceleration, thereby keeping their long axis quasi-parallel to the mainstream of the airflow. In the unstable session, i.e., the sudden 180° rotating session (see Figures 10(a) and 10(b)), the particle dramatically accelerates angularly. The angle between the z′- and x-axes, which is from 0° to 90°, is defined as

$$\alpha_i = \arccos\left|\cos(x, z')\right|. \tag{29}$$

Instead of using the magnitude of the angular velocity to define the onset of instability. The change-rate of $\cos\alpha_i$, which may also reflect the magnitude of the angular velocity, is introduced (see Figure 11(b)). The critical angle $\alpha_{cr}$ is the smallest angle which can be defined as

$$\left|d\left(\cos\alpha_i\right)/dt\right| \geq k_{cr}, \tag{30}$$

where $k_{cr}$ is the critical slope. In general, small $\alpha_{cr}$-values indicate that the particle is disturbed easily and hence its path may be destabilized, while larger $\alpha_{cr}$-values imply that the particle trajectory is more stable. In the extreme case of $\alpha_{cr} = 90°$, the particle is always stable and thereby avoiding any sudden 180° rotation.

#### 2. Determination of the critical slope $k_{cr}$

The critical slope value, here $1\ s^{-1} \le k_{cr} \le 10\ s^{-1}$, has a significant impact on the magnitude of the critical angle with respect to the particle release position as shown in Figure 11(a). Specifically, when $1\ s^{-1} \le k_{cr} \le 10\ s^{-1}$, the particle rotates in a high angular velocity, leading to a large change-rate in $\cos\alpha_i$. For an off-center position of $y_0^* \neq 0$, the critical angle $\alpha_{cr}$ increases with $k_{cr}$. In order to determine a reasonable value for $k_{cr}$, the threshold of unstable time interval $t_{cr}$, as determined by different $k_{cr}$ values (i.e., $k_{cr} = 1.0\ s^{-1}$, $5.0\ s^{-1}$, or $10.0\ s^{-1}$), are indicated in Figure 11(b) for an ellipsoidal particle with $a_p = 0.5\ \mu m$ and $\beta = 14$. It can be observed that $k_{cr} = 5.0\ s^{-1}$ provides the most reasonable threshold for defining the start of the unstable time interval. Specifically, as shown in Figure 11(b), $k_{cr} = 1.0\ s^{-1}$ is too early to indicate the threshold, as the particle orientation is still quasi-parallel to the mainstream, while $k_{cr} = 10.0\ s^{-1}$ is too late, because the particle's orientation has already started to change dramatically. In summary, the critical slope $k_{cr}$ should be defined as $5.0\ s^{-1}$, where the unstable time interval $t_{cr}$ is the interval duration between the onset and the end of the unstable session. Therefore, the critical angle $\alpha_{cr}$ is a convenient parameter to evaluate the stability of ellipsoidal particles with different shapes, subjected to different airflow field conditions.

#### 3. Stability impact of the initial release position

Different initial release positions imply different shear rates acting on the ellipsoidal particles, which determine different stabilities. The relationship between critical angle $\alpha_{cr}$ and different particle initial release positions are shown in Figure 11(a). It can be observed that for the particle which is released closer to the centerline of the circular tube, i.e., $|y_0^*| \le 0.18$, larger critical angles are possible. That indicates higher stability when compared to particles released further away from the centerline; because of the higher velocity gradients near the wall of the circular tube than around the centerline.

#### 4. Stability impact of the aspect ratio of the particle

Figure 11(c) presents the relationship between the critical angle $\alpha_{cr}$ and the aspect ratio $\beta$ of ellipsoidal particles for different inlet Reynolds numbers, i.e., $Re_{in} = 173$ and 559. With the increase in the particle's aspect ratio, the critical angle $\alpha_{cr}$ also increases, indicating that particles with higher aspect ratios, say, $\beta > 6$, are less likely to be disturbed or destabilized. Such geometric characteristics may influence the capability of the particle to follow the main flow. Also, for the higher inlet Reynolds number of $Re_{in} = 559$, smaller critical angles were observed. It can be explained that higher inlet Reynolds numbers generate higher velocity gradients at the same location, causing the particle to undergo an unstable stage during sedimentation and rotation.

### C. Revised Stokes diameter

Different effective- (or equivalent-) diameter methods can be found in the literature, e.g., the equivalent volume diameter,[51] Stokes equivalent diameter,[38] aerodynamic diameter,[52] etc. Associated with $d_{eff}$ are semi-empirical, non-spherical particle correlations for the drag force, lift force and other forces, as needed. When compared to the computer-intensive EL-ER method, a sufficiently accurate effective-diameter method can be very useful for the approximate analysis of non-spherical particle transport and deposition. However, existing effective diameter correlations do not provide accurate transport and deposition results for ellipsoidal particles (see Figures 12(a) and 12(b)). Hence, a revised Stokes diameter is proposed in this section and validated.

The conventional "equivalent-sphere" Stokes diameter expression is given by Shapiro and Goldenberg[53] in the form

$$d_{st} = 2a_p \sqrt{\frac{\beta \ln\left(\beta + \sqrt{\beta^2 - 1}\right)}{\sqrt{\beta^2 - 1}}}. \tag{31}$$

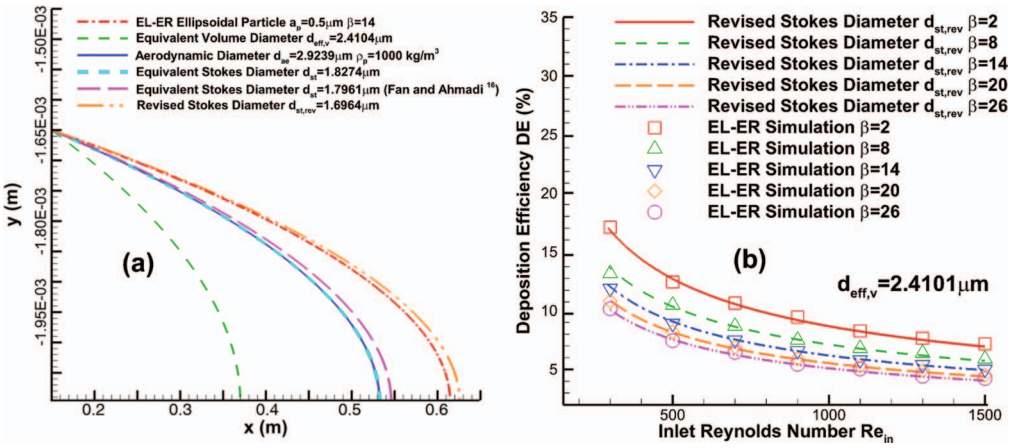


FIG. 12. (a) Trajectory comparisons between different equivalent diameter methods including the use of in-house revised Stokes diameter $d_{st,rev}$ and ellipsoidal particle transport and deposition for a single particle injected at x = 0.15 m, y = −0.00165 m, z = 0.0 m (b) deposition efficiency comparisons between ellipsoidal particle simulations and effective diameter method using in-house revised Stokes diameter $d_{st,rev}$.

Equation (31) was derived based on the probabilistic assumption that the three principal axes of the ellipsoidal particle are 33% of the time parallel to the flow direction. However, based on the experimentally validated simulation results, this assumption does not always hold. Specifically, Figure 10(a) shows that with an increase in a fiber's aspect ratio, the fiber will spend more and more time with the long axis being quasi-parallel to the mainstream airflow (i.e., over 33% of the time during the transport). In this case, the time-averaged ratio between the drag force component along the mainstream direction and the radial direction will be smaller than claimed by Shapiro and Goldenberg.[53] Hence, the fiber will be transported further when compared to a spherical particle with the same conventional Stokes diameter. This propensity to follow the mainstream flow (see Figure 10(b)) of the fiber is similar to spherical particles with smaller diameters than the classical Stokes diameter. Consequently, a correction function $f(\beta, Re_{in})$ has been introduced to revise the conventional Stokes diameter (Eq. (31)). The new revised Stokes diameter $d_{st,rev}$ is defined as

$$d_{st,rev} = f(\beta, Re_{in}) \cdot d_{st}, \tag{32}$$

where $d_{st}$ is given by Eq. (31). Because the function f is related to the rotational motion of the ellipsoidal particles, f should be a function of both inlet Reynolds number $Re_{in}$ and the aspect ratio $\beta$; specifically, when $\beta$ is equal to 1 indicating that the particle is spherical, $f(\beta, Re_{in})$ should be unity for any inlet Reynolds number $Re_{in}$. The expression for $f(\beta, Re_{in})$ was obtained via curve-fitting of numerical simulation results, yielding a coefficient of determination of 0.9446,

$$f(\beta, Re_{in}) = C_0 + C_1(\beta - 1) + C_2(\beta - 1) \cdot Re_{in} + C_3(\beta - 1)^2. \tag{33}$$

The coefficients $C_0$–$C_3$ are

$$C_0 = 1.0000, \tag{34a}$$

$$C_1 = -0.006722, \tag{34b}$$

$$C_2 = -2.9380 \times 10^{-6}, \tag{34c}$$

$$C_3 = 0.0001287. \tag{34d}$$

The Stokes diameter correction factor $f(\beta, Re_{in})$ (see Eq. (33)) holds for ellipsoidal particles in incompressible Newtonian fluid flow with aspect ratios $1 \le \beta \le 30$ and inlet Reynolds number

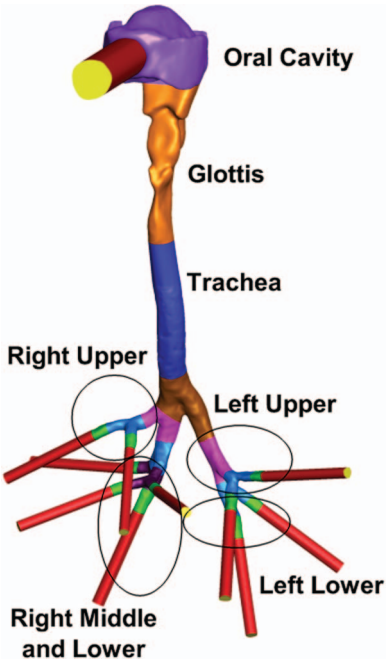


FIG. 13. Cast A's airway branches for each lung lobar.

$300 \leq \mathrm{Re}_{in} \leq 1500$. It was implied that the particle-to-fluid density ratio is larger than 500. Thus, certainly for airflow the density effect on the Stokes diameter correction is negligible.

The impact of the use of various effective diameters on the trajectories of a single particle, i.e., an ellipsoid, cylinder, or an equivalent sphere, is shown in Figure 12(a). Our in-house revised Stokes diameter provides the most accurate trajectories; hence, $d_{st,rev}$ is an effective quasi-spherical diameter device which is able to provide reasonable predictions for ellipsoidal particle transport and deposition in circular tubes.

Figure 12(b) presents a comparison for deposition efficiencies of ellipsoidal particles with different inlet Reynolds numbers ($300 \leq \mathrm{Re}_{in} \leq 1500$) and aspect ratios ($2 \leq \beta \leq 26$) in tubular Poiseuille flow, considering both numerical simulations with the rotation equations and the effective diameter method with the new revised Stokes diameter $d_{st,rev}$. Clearly, using $d_{st,rev}$ as the effective diameter, numerical simulation results agree very well with the ellipsoidal particle simulations. As expected, the deposition efficiency decreases with an increase in $\mathrm{Re}_{in}$ and $\beta$.

### D. Particle transport and deposition in a subject-specific human respiratory system

The availability of an actual physical model (Cast A) and associated fiber-deposition measurements provides by the Loveless Respiratory Research Institute (LRRI, Albuquerque, NM) allowed for comparisons, based on the outlined theories for both non-spherical particle and approximate equivalent-sphere dynamics.

#### *1. Geometry*

The stereo-lithography (STL) file of the human airway model (see Figure 13) was generated using NextEngine's Desktop 3D Scanner and processed with ScanStudio software (NextEngine Inc., Santa Monica, CA). The prototype of the human airway model (Cast A with mouth-tube for proper inlet conditions) extends from the oral cavity to lung airway generation 4. It is a wax replica which is the same one as used in the experimental study by Su and Cheng,[26] who developed it from *in vivo* measurements (oral cavity) and cadavers (trachea-bronchial section).

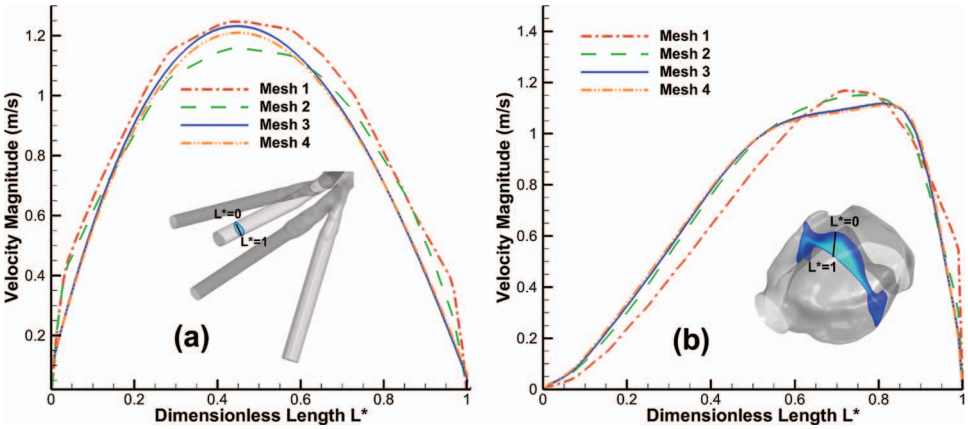


FIG. 14. (a) Mesh independence test for Cast A: velocity profiles at the cross-section in the oral cavity (b) Mesh independence test for Cast A: Velocity profiles at the cross-section in lung airway cross-section near the outlet.

### 2. Mesh generation and independence test

The mesh independence and sensitivity tests were performed using steady flow simulations with an inlet volume flow rate of $Q_{in} = 15$ L/min. The SST transition model was employed. The no-slip wall boundary condition was invoked and the outlet pressures were set to be uniform. A specified solver RMS residual was defined to be less than $1.0 \times 10^{-6}$. Mesh-independence was investigated by comparison of velocity profiles at a few selected locations from mouth to generation G5 as shown in Figures 14(a) and 14(b). Detailed information on Mesh 1–Mesh 4 was documented in Ref. 32. The final mesh (Mesh 3) contained 10 131 966 elements and 2 428 246 nodes, with 6 prism layers placed at the wall.

### 3. Transitional airflow field

In order to understand and visualize the complex airflow field in Cast A, cross-sections from 1-1′ to 21-21′ were selected and their locations are shown in Figure 15, including the sagittal plane at $z = 0$ from mouth-inlet to the 1st bifurcation. Figure 15 represents the contour of the nondimensionalized velocity magnitude and stream-traces of the transitional airflow in the sagittal plane (i.e., $z = 0$) as well as cross-sections along the human respiratory tract. The case of $Q_{in} = 60$ L/min is used to show the complex laminar-to-turbulent flow field characteristics. It can be observed that the maximum airflow velocity is at the glottis, being approximately 4.58 times of the inlet velocity (i.e., 3.009 m/s in the $Q_{in} = 60$ L/min case) due to the sudden local contraction. Furthermore, the high-velocity jet in the glottis is visualized which also depicts streamlines with several recirculation regions; especially, near the upper palate, below the glottis, and at the back of the trachea near the 1st bifurcation. Figure 15 also depicts the impaction of the main stream in the curved region between the oral cavity and the oropharynx because of the centrifugal force. The highly asymmetric and complex secondary flows, especially in the oral cavity, oropharynx, and larynx, are visualized with streamlines as well.

Secondary flows shown in Figure 15 will have a significant influence on the transport and deposition of fibers and particles in Cast A. The secondary airflows, such as a pair of counter rotating vortices formed in the oral cavity, qualitatively agree well with experimental observations, where however somewhat different human respiratory system geometries were used.[54–56] The dominant patterns in the sagittal plane of Cast A are: (a) recirculation behind the teeth; (b) recirculation around the epiglottis; (c) laryngeal turbulent jet flow; (d) recirculation after the glottis; and relaminarization, typically after generation 2 depending on the inlet flow rate.

### 4. Particle deposition

The impact of inhaled particle deposition in the subject-specific human airway model is shown in Figures 16–18. Since the validity of using steady-state inlet condition to approximate real transient

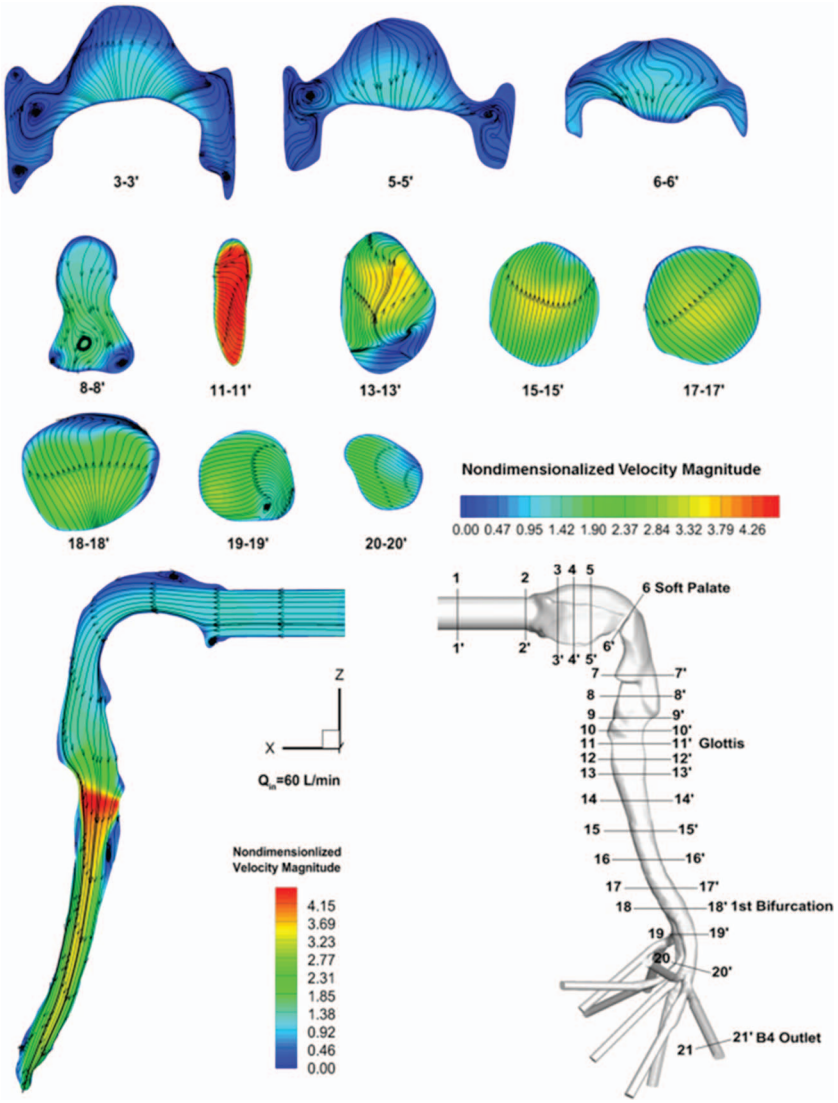


FIG. 15. Nondimensionalized velocity contour and stream-traces in sagittal plane z = 0 and different cross-sections of Cast A for $Q_{in}$ = 60 L/min.

airflow field in human respiratory system has been discussed by Zhang and Kleinstreuer,[57] steady-state inlet conditions are employed (i.e., 15–60 L/min). EL-ER method and effective diameter method using the revised Stokes diameter (Eq. (34)) were employed. About 100 000 randomly selected, uniformly distributed fibers were released at the mouth-inlet in order to assure that the deposition profiles were independent of the particle count.

In Figure 16, the revised Stokes diameter method and the EL-ER method are compared to the Cast A experimental data of Su and Cheng[26] in terms of overall particle-deposition values for an inhalation flow rate of 15 L/min. The ellipsoidal test particles all have the same minor axis (i.e., $a_p$ = 1.83 $\mu$m) but different aspect ratios (i.e., $\beta$ ranges from 2.73 to 27.3). As a result, with increasing $\beta$, implying higher $b_p$-values, the particle's volume increases and its shape becomes needle-like. When compared to the experimental data with error bars, the numerical results for methods (i.e., EL-ER and revised Stokes diameter) show the right trend for DE ($\beta$), i.e., an increase because of enhanced inertial impaction. Still, there are differences in DE-magnitudes which can be explained as follows:

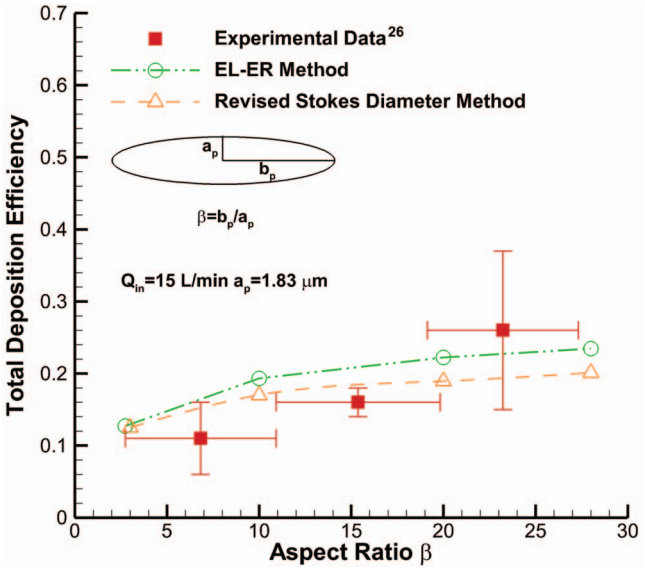


FIG. 16. Total deposition efficiency comparisons for the subject-specific human respiratory model (Cast A) between revised Stokes diameter method, EL-ER method, and experimental data with error bars.[26]

a. *Different initial particle diameter distribution:* Su and Cheng[26] claimed that particles released at the inlet were not mono-dispersed, while for the numerical study the injected particles had a uniform diameter.
b. *Different particle shapes*: Fibers used in the measurements were approximated as thin ellipsoids in the numerical study.
c. *Differences in geometry reconstruction of the physical oral-cavity and lung-airway wax models:* The STL file of Cast A was generated by combining the oral cavity part and the lung airway part as smoothly as possible; however, the geometry of Cast A employed in the numerical simulation may not be identical to the one used in the experiments.

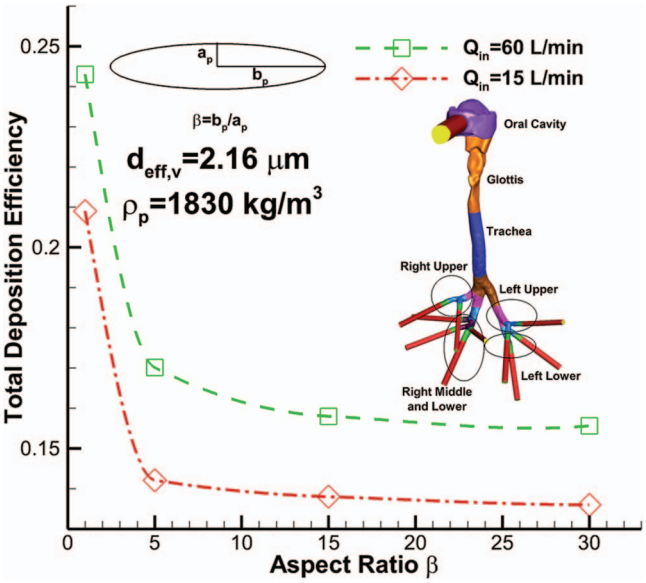


FIG. 17. Total deposition efficiencies of ellipsoidal particles, including spheres ($\beta = 1.0$), at two inhalation flow rates in a subject-specific lung airway model as a function of aspect ratio.

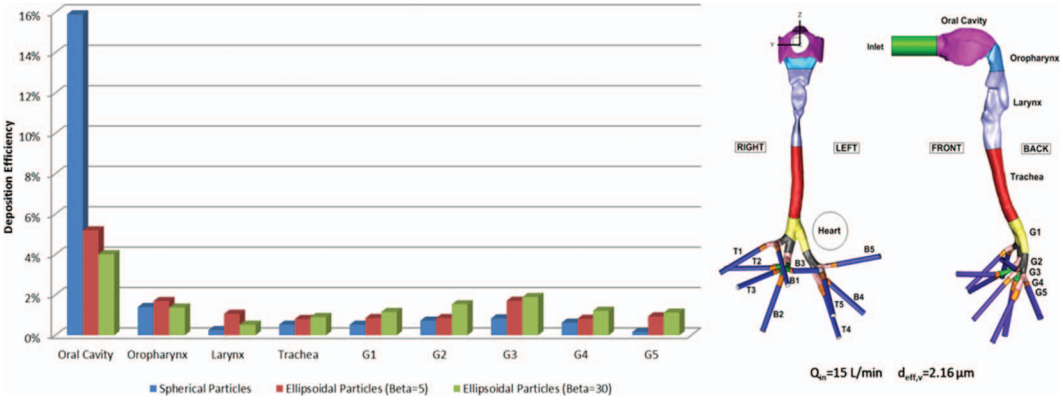


FIG. 18. Comparison of deposition efficiencies for particles with different aspect ratios ($\beta$).

d. *Particle agglomeration:* In the present numerical study particle agglomeration was neglected. Although the particle suspension was assumed to be dilute, agglomeration cannot be fully avoided during experiments, which may have had an impact on the deposition efficiency in Cast A.
e. *Unexpected disturbances in the laboratory airflow field:* Airflow disturbances will influence the deposition probabilities of particles which may contribute to the DE difference between experiment and simulation. For example, the airflow perturbation caused by the air pump may not provide perfectly a steady inlet flow rate during the experimental period.

A comparison of total deposition efficiencies of spheres and ellipsoidal particles for two inhalation flow rates is shown in Figure 17. The results of the validated computer simulation model clearly indicate that ellipsoidal particles with high aspect ratios become thin elongated fibers as $b_p$ increases, which implies $a_p \sim b_p^{-1/2}$ because the volume was kept constant. Such nano-needles are more dangerous than spherical particles or particles with low aspect ratios, due to their ability to penetrate into deeper lung airways, when they line up with the axial flow. Furthermore, the effect of inlet flow rate on particle deposition is also shown in Figure 17, which indicates that ellipsoidal particle deposition is enhanced as the breathing rate increases.

Local deposition comparisons between particles of the same volume but different aspect ratios ($\beta = 1$, 5, and 30) are shown in Figure 18. In the upper respiratory system the deposition efficiency of inhaled particles decreases significantly, especially in the oral cavity with increasing particle aspect ratio. However, in the lung airways (i.e., from the trachea to generation 4) for inhaled particles with higher aspect ratios the deposition efficiency increases slightly. Such interesting phenomena indicate that in the upper lung airways impaction is the major mechanism for particle deposition, while in the bronchial airways, especially in higher generation branches, interception due to strong secondary flows is the most significant mechanism for particle deposition.

### 5. Revised Stokes diameter method

Total deposition efficiencies when using the revised Stokes diameter method were already shown in Figure 16. Local deposition efficiencies for the effective diameter methods and the EL-ER method are given in Figures 19(a) and 19(b), selecting an inlet flow rate of 15 L/min and ellipsoidal particles with two different aspect ratios, i.e., $\beta = 5$ and $\beta = 30$. Concerning the different effective diameter methods, it can be concluded that using the revised Stokes diameter (see Eq. (33)) provides a better DE prediction from the oral cavity to the larynx in Cast A than using the effective volume diameter or conventional Stokes diameter.[53] However, although the revised Stoke diameter method is able to provide accurate deposition prediction in Poiseuille flow (see Figures. 12(a) and 12(b)), it is not able to predict the deposition efficiency of ellipsoidal particles from G1 to G5 more accurately than with the effective volume diameter. Thus, the following observations can be made:

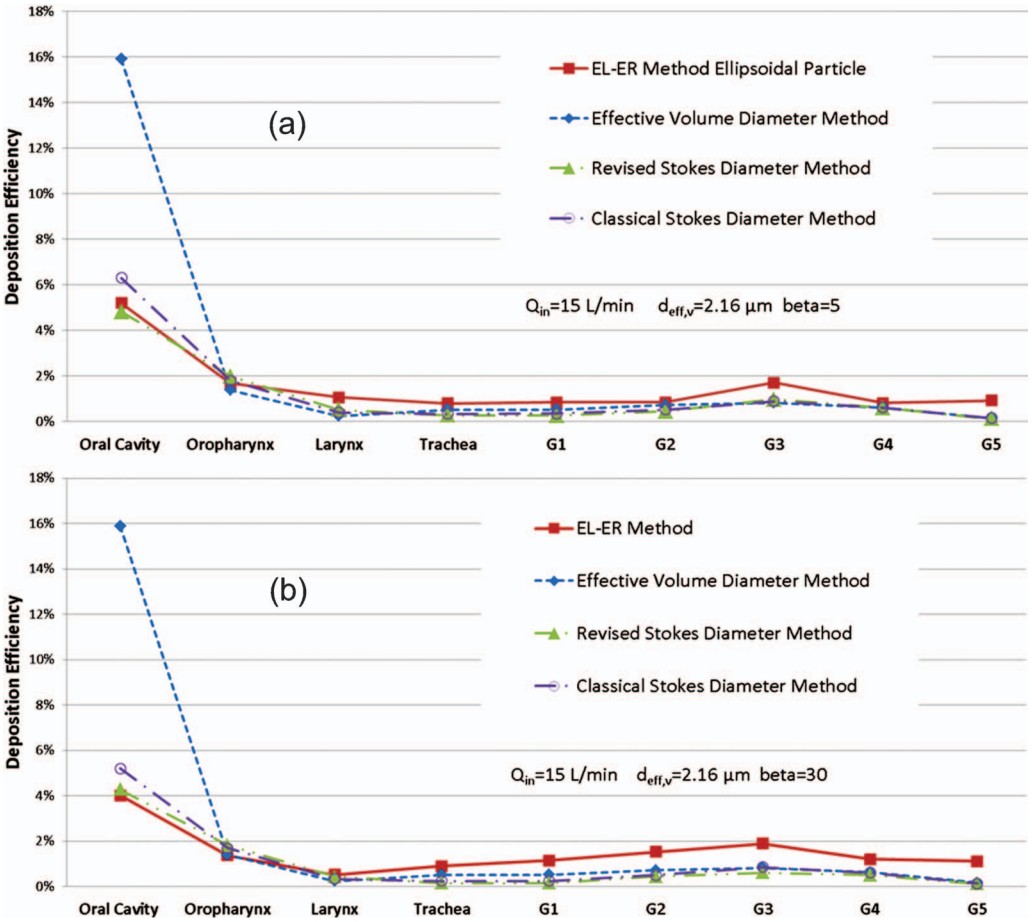


FIG. 19. Local deposition efficiencies comparing EL-ER method with different effective diameter methods using ellipsoids with: (a) $\beta = 5$; and (b) $\beta = 30$.

a. The major deposition mechanism in the oral cavity is impaction and sedimentation, while the airflow field is laminar. Such circumstances are similar to ellipsoidal particle deposition in Poiseuille flow. Hence, the revised Stokes diameter method can provide accurately prediction in basic shear flows.
b. The major deposition mechanism for ellipsoidal particles in small lung airways is interception. If the revised Stokes diameter is employed in such complex shear flows, treating elongated ellipsoids as spheres will change the interception mechanism significantly. That leads to DE differences between the EL-ER method and the revised Stokes diameter method. This can be also observed in Figures. 18(a) and 18(b) where for particles with aspect ratios from 5 to 30 the

TABLE I. Numerical simulation CPU time comparisons between revised Stokes diameter method and EL-ER method for selected cases (number of particle released = 10 000)[a]

| Inlet flow rate (L/min) | Particle aspect ratio | Revised Stokes diameter method (h) | EL-ER method (h) |
|---|---|---|---|
| $Q_{in} = 15$ | $\beta = 5$ | 1.83 | 13.35 |
| $Q_{in} = 15$ | $\beta = 30$ | 4.20 | 38.59 |
| $Q_{in} = 60$ | $\beta = 5$ | 0.12 | 1.00 |
| $Q_{in} = 60$ | $\beta = 30$ | 0.26 | 2.35 |

[a]The numerical simulations were performed on a local Dell Precision T3500 workstation with 12 GB RAM and 4 3.33 GHz CPUs.

predicted deposition differences between EL-ER method and revised Stokes diameter method further increase.

Additionally, computational costs are given in Table I. The simulation CPU time comparisons between the two methods show that using the revised Stokes diameter method requires much less CPU time (i.e., $O(0.1)$) when compared to the EL-ER method.

## IV. CONCLUSIONS

A computational model was developed for ellipsoidal particle transport and deposition, considering the impact of anisotropic shape effects on non-spherical particle dynamics in shear flows. Transport characteristics of ellipsoidal particles in Poiseuille flow were investigated and analyzed with new physical insight. A revised Stokes diameter for ellipsoidal particles is proposed which can more accurately predict non-spherical particle transport and deposition. Applied to ellipsoidal particle transport and deposition in a human respiratory system, acceptable results have been obtained with much lower computational cost when compared to the EL-ER method. Concerning non-spherical particle transport and deposition in a subject-specific respiratory system, the validated computer simulation model provides realistic and accurate particle-deposition results. Specifically, slender non-spherical particles (i.e., those with higher aspect ratios) are more dangerous than thicker ones due to their ability to penetrate into deeper lung regions when aligned with the major flow field. Furthermore, non-spherical particle deposition is enhanced as the breathing rate increases.

## ACKNOWLEDGMENTS

The authors are grateful for the supply of the physical cast-model by Dr. W. C. Su (LRRI, Albuquerque, NM), the use of the NextEngine Desktop 3D Scanner at NCSU as arranged by Professor J. Strenkowski, and the assistance of Mr. D. Thomas (Material Science Dept., NCSU) and of Dr. J. Li (MAE Dept., NCSU) in STL-file generation. The use of ANSYS software (Canonsburg, PA) as part of the ANSYS-NCSU Professional Agreement is gratefully acknowledged, as well as the financial support of Y.F. by a grant from NSF (CBET-1232988), Environmental Health and Safety of Nanotechnology, Dr. Barbara Karn, Program Director.

[1] Z. Wang, P. K. Hopke, P. A. Baron, G. Ahmadi, Y. S. Cheng, G. Deye, and W. C. Su, "Fiber classification of the influence of average air humidity," Aerosol Sci. Technol. **39**, 1056–1063 (2005).
[2] L. Tian, G. Ahmadi, Z. Wang, and P. K. Hopke, "Transport and deposition of ellipsoidal fibers in low Reynolds number flows," J. Aerosol Sci. **45**, 1–18 (2012).
[3] R. Sturm and W. Hofmann, "A theoretical approach to the deposition and clearance of fibers with variable size in the human respiratory tract," J. Hazard. Mater. **170**, 210–218 (2009).
[4] S. E. Gratton, P. A. Ropp, P. D. Pohlhaus, J. S. Luft, V. J. Madden, M. E. Napier, and J. M. Desimone, "The effect of particle design on cellular internalization pathways," Proc. Natl. Acad. Sci. U.S.A. **105**, 11613–11618 (2008).
[5] C. W. Lam, J. T. James, R. Mccluskey, S. Arepalli, and R. L. Hunter, "A review of carbon nanotube toxicity and assessment of potential occupational and environmental health risks," Crit. Rev. Toxicol. **36**, 189–217 (2006).
[6] I. Fenoglio, E. Aldieri, E. Gazzano, F. Cesano, M. Colonna, D. Scarano, G. Mazzucco, A. Attanasio, Y. Yakoub, D. Lison, and B. Fubini, "Thickness of multi-walled carbon nanotubes affects their lung toxicity," Chem. Res. Toxicol. **25**, 74–82 (2012).
[7] D. W. Kamp, "Asbestos-induced lung diseases: An update," Trans. Res. **153**(4), 143–152 (2009).
[8] M. R. Gwinn, D. Devoney, A. M. Jarabek, B. Sonawane, J. Wheller, D. N. Weissman, S. Masten, and C. Thompson, "Meeting report: Mode(s) of action of asbestos and related mineral fibers," Environ. Health Perspect. **119**(12), 1806–1810 (2011).
[9] M. Pacurari, Y. Qian, D. W. Porter, M. Wolfarth, Y. Wan, and D. Luo, "Multi-walled carbon nanotube-induced gene expression in the mouse lung: Association with lung pathology," Toxicol. Appl. Pharmacol. **255**(1), 18–31 (2011).
[10] C. Kleinstreuer and Y. Feng, "Computational analysis of non-spherical particle transport and deposition in shear flow with application to lung aerosol dynamics – A review," ASME J. Biomech. Eng. **135**(2), 021007-1–021007-19 (2013).
[11] E. A. Simone, T. D. Dziubla, and V. R. Muzykantov, "Polymeric carriers: Role of geometry in drug delivery," Expert Opin. Drug Deliv. **5**(12), 1283–1300 (2008).
[12] C. Kleinstreuer, E. M. Childress, and A. S. Kennedy, "Targeted drug delivery: Multifunctional nanoparticles and direct micro-drug delivery to tumors," *Transport in Biological Media*, edited by S. Becker and A. Kuznetsov (Elsevier, London, 2012), Chap. 10.
[13] G. B. Jeffery, "The motion of ellipsoidal particles immersed in a viscous fluid," Proc. R. Soc. London A **102**, 161–179 (1922).

[14] I. Gallily and A. D. Eisner, "On the orderly nature of the motion of nonspherical aerosol particles: I. Deposition from a Laminar flow," J. Colloid Interface Sci. **68**(2), 320–337 (1979).
[15] Y. K. Chen and C. P. Yu, "Sedimentation of fibers from Laminar flows in a horizontal circular duct," Aerosol Sci. Technol. **14**, 343–347 (1991).
[16] F. G. Fan and G. Ahmadi, "A sublayer model for wall deposition of ellipsoidal particles in turbulent streams," J. Aerosol Sci. **26**(5), 813–840 (1995).
[17] K. T. Shanley and G. Ahmadi, "A numerical model for simulating the motion of ellipsoidal fibers suspended in low Reynolds number shear flows," Aerosol Sci. Technol. **45**, 838–848 (2011).
[18] C. Yin, L. Rosendahl, S. K. Kaer, and H. Sorensen, "Modeling the motion of cylindrical particle in a nonuniform flow," Chem. Eng. Sci. **58**, 3489–3498 (2003).
[19] S. M. Hoegberg, "Particle transport in human lung-effects of particle size and shape," Licentiate Thesis (Luleå University of Technology, Luleå, Sweden, 2008).
[20] J. K. Comer and C. Kleinstreuer, "Computational analysis of convection heat transfer to non-spherical particles," Int. J. Heat Mass Transfer **38**(17), 3171–3180 (1995).
[21] T. Myojo, "Deposition of fibrous aerosol in model bifurcating tubes," J. Aerosol Sci. **18**, 337–347 (1987).
[22] T. Myojo, "The effect of length and diameter on deposition of fibrous aerosol in a model lung bifurcation," J. Aerosol Sci. **21**(5), 651–659 (1990).
[23] T. Myojo and M. Takaya, "Estimation of fibrous aerosol deposition in upper bronchi based on experimental data with model bifurcation," Ind. Health **39**, 141–149 (2001).
[24] E. R. Weibel, "Principles and methods for the morphometric study of the lung and other organs," Lab. Invest. **12**, 131 (1963).
[25] J. Marijnissen, A. Zeckendorf, S. Lemkowitz, and H. Bibo, "Transport and deposition of uniform respirable fibres in a physical lung model," J. Aerosol Sci. **22**(1), S859–S862 (1991).
[26] W. C. Su and Y. S. Cheng, "Fiber deposition pattern in two human respiratory tract replicas," Inhalation Toxicol. **18**(10), 749–760 (2006).
[27] W. C. Su and Y. S. Cheng, "Deposition of man-made fibers in human respiratory airway casts," J. Aerosol Sci. **40**, 270–284 (2009).
[28] Y. Zhou, W. C. Su, and Y. S. Cheng, "Fiber deposition in the tracheobronchial region: Deposition equations," Inhalation Toxicol. **20**(13), 1191–1198 (2008).
[29] R. G. Sussman, B. S. Cohen, and M. Lippmann, "Asbestos fiber deposition in a human tracheobronchial cast: I. Experimental," Inhalation Toxicol. **3**, 145–160 (1991).
[30] H. I. Andersson, L. Zhao, and M. Barri, "Torque-coupling and particle–turbulence interactions," J. Fluid Mech. **1**(1), 1–11 (2012).
[31] H. Goldstein, C. P. Poole, and J. Safko, *Classical Mechanics* (Addison-Wesley Pub. Co., London, 2001).
[32] Y. Feng, "Non-spherical particle dynamics analysis with applications to inhaled aerosol transport and deposition in human upper airway models," Ph.D. dissertation (NC State University, Raleigh, NC, 2013).
[33] Z. Zhang and C. Kleinstreuer, "Laminar-to-turbulent fluid-nanoparticle dynamics simulations: Model comparisons and nanoparticle-deposition applications," Int. J. Numer. Methods Biomed. Eng. **27**, 1930–1950 (2011).
[34] Z. Zhang, C. Kleinstreuer, and S. Hyun, "Size-change and deposition of conventional and composite cigarette smoke particles during inhalation in a subject-specific airway model," J. Aerosol Sci. **46**, 34–52 (2012).
[35] Y. Wang and P. W. James, "On the effect of anisotropy on the turbulent dispersion and deposition of small particles," Int. J. Multiphase Flow **25**, 551–558 (1999).
[36] E. A. Matida, W. H. Finlay, C. F. Lange, and B. Grgic, "Improved numerical simulation of aerosol deposition in an idealized mouth-throat," J. Aerosol Sci. **35**, 1–19 (2004).
[37] A. R. Shenoy and C. Kleinstreuer, "Flow over a thin circular disk at low to moderate Reynolds numbers," J. Fluid Mech. **605**, 253–262 (2008).
[38] M. Mando and L. Rosendahl, "On the motion of non-spherical particles at high Reynolds number," Powder Technol. **202**, 1–13 (2010).
[39] E. Michaelides, "Hydrodynamic force and heat/mass transfer from particles, bubbles, and drops-the Freeman scholar lecture," J. Fluids Eng. **125**, 209–238 (2003).
[40] R. Clift, J. R. Grace, and M. E. Weber, *Bubbles, Drops, and Particles* (Dover Publications, Inc., Mineola, NY, 2005).
[41] E. Loth, "Drag of nano-spherical solid particles of regular and irregular shape," Powder Technol. **182**, 342–353 (2008).
[42] H. Brenner, "The Stokes resistance of an arbitrary particle," Chem. Eng. Sci. **18**, 1–25 (1963).
[43] A. Hölzer and M. Sommerfeld, "New simple correlation formula for the drag coefficient of non-spherical particles," Powder Technol. **184**(3), 361–365 (2008).
[44] A. Richter and P. A. Nikrityuk, "Drag forces and heat transfer coefficients for spherical, cuboidal and ellipsoidal particles in cross flow at sub-critical Reynolds numbers," Int. J. Heat Mass Transfer **55**, 1343–1354 (2012).
[45] S. F. Hoerner, *Fluid-Dynamic Drag: Practical Information on Aerodynamic Drag and Hydrodynamic Resistance* (self-published, Midland Park, NJ, 1965).
[46] E. Y. Harper and I. Chang, "Maximum dissipation resulting from lift in a slow viscous shear flow," J. Fluid Mech. **33**(2), 209–225 (1968).
[47] D. A. Drew and R. T. Lahey, Jr., "The virtual mass and lift force on a sphere in rotating and straining flow," Int. J. Multiphase Flow **25**(6/7), 1321–1372 (1987).
[48] T. R. Auton, "The lift force on a spherical body in a rotational flow," J. Fluid Mech. **183**, 199–218 (1987).
[49] P. W. Longest and J. Xi, "Effectiveness of direct Lagrangian tracking models for simulating nanoparticle deposition in the upper airways," Aerosol Sci. Technol. **41**, 380–397 (1990).
[50] L. Zhang, B. Asgharian, and S. Anjilvbel, "Inertial and interceptional deposition of fibers in a bifurcating airway," J. Aerosol Sci. **9**(3), 419–532 (1996).

[51] B. R. Jennings, K. Parslow, B. R. Jennings, and K. Parslow, "Particle size measurement: The equivalent spherical diameter," Proc. R. Soc. London, Ser. A **419**(1856), 137–149 (1988).
[52] S. M. Hoegberg, H. O. Akerstedt, T. S. Lundstroem, and J. B. Freund, "Respiratory deposition of fibers in the non-inertial regime-development and application of a semi-analytical model," Aerosol Sci. Technol. **44**, 847–860 (2010).
[53] M. Shapiro and M. Goldenberg, "Deposition of glass fiber particles from turbulent air flow in a pipe," J. Aerosol Sci. **24**(1), 65–87 (1993).
[54] A. Johnstone, M. Uddin, A. Pollard, A. Heenan, and W. H. Finlay, "The flow inside an idealised form of the human extra-thoracic airway," Exp. Fluids **37**, 673–689 (2004).
[55] S. T. Jayaraju, M. Brouns, C. Lacor, B. Belkassem, and S. Verbanck, "Large Eddy and detached Eddy simulations of fluid flow and particle deposition in a human mouth-throat," J. Aerosol Sci. **39**(10), 862–875 (2008).
[56] A. Pollard and A. M. Shinneeb, "Oro-pharangeal-laryngeal flow physics," in *Proceedings of the 17th Australasian Fluid Mechanics Conference, Auckland, New Zealand* (Curran Associates Inc., Red Hook, NY, 2011), p. 861.
[57] Z. Zhang and C. Kleinstreuer, "Transient airflow structures and particle transport in a sequentially branching lung airway model," Phys. Fluids **14**, 862 (2002).